photonics

MDPI

Article

Inverse Judd–Ofelt Formalism Based on Radiative Lifetime for Comparative Spectroscopy of RE^{3+} Ions in Glass

Helena Cristina Vasconcelos [1,2,*], **Maria Gabriela Meirelles** [1,3] **and Reşit Özmenteş** [4]

[1] Faculty of Science and Technology, University of the Azores, S. Miguel, Azores, 9500-321 Ponta Delgada, Portugal; maria.gf.meirelles@uac.pt
[2] Laboratory of Instrumentation, Biomedical Engineering and Radiation Physics (LIBPhys, UNL), Department of Physics, NOVA School of Science and Technology, 2829-516 Caparica, Portugal
[3] Research Institute of Marine Sciences of the University of the Azores (OKEANOS), Faial, Azores, 9901-862 Horta, Portugal
[4] Vocational School of Health Services, Bitlis Eren University, 13100 Bitlis, Turkey; ozmentes@gmail.com
* Correspondence: helena.cs.vasconcelos@uac.pt

Abstract

This work shows that inverse Judd–Ofelt (JO) analysis of relative absorption spectra, anchored by a single lifetime, provides JO parameters and radiative rates without absolute calibration. The method is applied to Er^{3+}, Dy^{3+}, and Sm^{3+} in a compositionally identical oxyfluoride glass. Three well-resolved ground-state 4f–4f absorption bands were selected. After baseline removal and wavenumber-domain integration, their normalized strengths $S_{\mathrm{rel,k}}$ (k = 1, 2, 3; k∈S) define a 3 × 3 system solved by non-negative least squares to obtain the anchor-independent ordering (Ω_2:Ω_4:Ω_6). Absolute scaling uses a single lifetime anchor. We report lifetime-scaled Ω_t and A_{rad}, and the normalized fractions p_k within the selected triplets; as imposed by the method, the anchor-independent ordering (Ω_2:Ω_4:Ω_6) is analyzed, while absolute A_{rad} and Ω_t scale with τ_{ref}. The extracted parameters fall within the expected ranges for oxyfluoride hosts and reveal clear ion-specific trends: Ω_2 follows $Dy^{3+} > Er^{3+} > Sm^{3+}$ (site asymmetry/hypersensitive response), while the ordering $\Omega_4 > \Omega_6$ holds across all ions (oxide-rich networks). Er^{3+} exhibits the largest Ω_4 and the smallest Ω_6, indicative of pronounced medium-range "rigidity" with suppressed long-range polarizability; Sm^{3+} shows the lowest Ω_2 (more symmetric/less covalent coordination); and Dy^{3+} the highest Ω_2 (strong hypersensitive behavior). Uncertainty was quantified by Monte Carlo resampling of the preprocessing steps, yielding compact 95% confidence intervals; the resulting JO-parameter trends (Ω_2, Ω_4, Ω_6) and normalized f_k fractions reproduce the characteristic spectroscopic behavior known for each ion. This method enables quantitative JO outputs from uncalibrated spectra, allowing direct spectroscopic comparisons and quick screening when only relative absorption data are available.

Keywords: inverse Judd–Ofelt analysis; Judd–Ofelt parameters (Ω_2, Ω_4, Ω_6); Einstein radiative coefficients (A_{rad}); normalized ED fraction f_k; radiative lifetime anchor (τ_{ref}); 4f–4f absorption spectroscopy; rare-earth-doped oxyfluoride glass; erbium (Er^{3+}); dysprosium (Dy^{3+}); samarium (Sm^{3+})

check for updates

Received: 25 August 2025
Revised: 7 October 2025
Accepted: 11 October 2025
Published: 13 October 2025

Citation: Vasconcelos, H.C.; Meirelles, M.G.; Özmenteş, R. Inverse Judd–Ofelt Formalism Based on Radiative Lifetime for Comparative Spectroscopy of RE^{3+} Ions in Glass. *Photonics* **2025**, *12*, 1011. https://doi.org/10.3390/photonics12101011

1. Introduction

Rare-earth (RE^{3+})-doped materials occupy a central position in photonics owing to their sharp intra-4f electronic transitions, partially shielded from the host environment by outer 5s and 5p orbitals. This shielding produces spectrally narrow, chemically stable absorption and emission lines—a combination difficult to match with other dopants—making RE^{3+} ions indispensable in lasers, optical amplifiers, phosphors, displays, and biomedical imaging systems [1,2]. Specifically relevant is that the 4f multiplet energies are nearly host-independent, while transition intensities remain strongly host-sensitive.

Technologically significant cases include erbium (Er^{3+}), whose $^4I_{13/2} \rightarrow {}^4I_{15/2}$ transition near 1500 nm supports telecom-band amplification; dysprosium (Dy^{3+}), which offers complementary blue–yellow emission channels for white-light generation; and samarium (Sm^{3+}), valued for its intense orange–red emission in display and sensing technologies [3,4].

The optical performance of RE^{3+}-doped systems is intimately linked to the local coordination environment of the dopant ions within the host lattice. In the 1960s, Judd and Ofelt [5,6] resolved the long-standing problem of intensity transfer by showing that odd-parity crystal-field components mix 4f states of opposite parity, thereby relaxing the Laporte rule and allowing electric–dipole transitions to acquire measurable intensity. The Judd–Ofelt (JO) theory [5,6] provides a unified framework for describing such behavior, expressing electric–dipole (ED) line strengths through three phenomenological parameters, Ω_2, Ω_4, and Ω_6. Beyond their role in calculating Einstein radiative coefficients A_{rad} (spontaneous emission probabilities), branching ratios (β), and radiative lifetimes, these parameters also serve as structural probes: Ω_2 reflects local asymmetry and 4f–ligand covalency; Ω_4 is linked to intermediate-range network rigidity; and Ω_6 captures long-range polarizability [7]. In this study, attention is restricted to electric–dipole (ED)-dominated transitions, since the selected bands in these glasses have negligible magnetic–dipole (MD) contributions. In most RE^{3+}-doped oxide and oxyfluoride glasses, the 4f–4f transitions employed in JO analysis are predominantly ED in character, with magnetic–dipole (MD) contributions comparatively small in the relevant spectral regions [8–10].

In the selected windows, MD contributions are small; at such levels, they primarily affect the absolute scale of radiative probabilities and do not alter the Ω-ratios or the normalized fractions pk within our reported uncertainty.

Under these conditions, the experimental line strengths can be directly related to the squared reduced matrix elements $\langle J_g \| U^{(t)} \| J_u \rangle$ (t = 2, 4, 6), which quantify the coupling between the ground (g) and upper (u) 4f multiplets for each tensor rank (multipole order). Extensive tabulations of these quantities for RE^{3+} ions in the free-ion/LaF_3 benchmark [10] provide a practical baseline for Judd–Ofelt analysis. However, where reliable host-specific reduced matrix elements $\langle U^{(t)} \rangle^2$ are available, they should be preferred [11]. In this comparative study, we adopt a single reference set (Carnall's LaF_3 tables) for Er^{3+}, Dy^{3+}, and Sm^{3+} solely to maintain cross-ion consistency within the same glass; the host dependence is then captured by the Ω_t parameters rather than by mixing heterogeneous U-tables across ions.

The classical JO formalism requires absolute oscillator strengths from calibrated absorption spectra, together with the sample thickness (d), dopant number density (N), and refractive index (n). While this is feasible in benchmark systems [8,9], exploratory glass compositions and small-batch samples often lack reliable thickness and concentration measurements.

Several methodological adaptations have been developed to circumvent these limitations. Diffuse-reflectance spectroscopy, combined with fluorescence lifetime measurements, enables recovery of Ω_t values without transmission data, even in powdered samples [12]. Emission-based strategies provide another route: the JOES (Judd–Ofelt Emission Spectroscopy) was developed to extract parameters directly from Eu^{3+} emission spectra [13], while a self-referenced excitation method has been proposed to internally normalize excitation intensities and thus avoid absolute calibration [14]. Modified formalisms have also been applied to Pr^{3+}-doped fluoride glasses, where normalization against lifetime data improved consistency between calculated and experimental results [15]. Goldner and Auzel [16] carried out a systematic comparison between the standard JO framework and a modified version incorporating normalized oscillator strengths in Pr^{3+}-doped fluorozirconate glasses. Their study showed that such normalization not only improved agreement between calculated and experimental lifetimes, but also mitigated the strong dependence of JO parameters on the set of transitions chosen for fitting—a recurrent difficulty in Pr^{3+} systems. This work remains an important reference, as it demonstrated that careful adaptation of this formalism can substantially enhance the reliability of JO analyses in hosts where absolute calibration of absorption spectra is challenging. Extensions of the methodology to nanocrystalline hosts further highlight its flexibility, as shown by Hien et al. [17] in their analysis of Dy^{3+}-doped $CoAl_2O_4$, where spectroscopic parameters were explicitly linked to local structural features.

More recently, "inverse" JO methodologies have been developed, in which relative absorption data are first used to determine Ω_2:Ω_4:Ω_6 ratios, and a single lifetime measurement is subsequently applied to fix the absolute scale. Notable examples include Xue et al. [18], who applied a diffuse-reflectance/Kubelka–Munk approach, extracting JO parameters from uncalibrated powder spectra by combining them with the radiative lifetime of a well-defined transition, thereby anchoring the absolute scale. Likewise, Vega et al. [19] applied a transmission-based strategy in Er^{3+}/Yb^{3+}-doped $BaTiO_3$, obtaining relative parameters from absorption spectra and enforcing absolute scaling through a predominantly radiative emission channel. Despite differing in experimental modality, both studies converge on the same underlying principle: the decoupling of relative parameter ratios from absolute scaling, a concept that provides the basis for the systematic multi-ion implementation presented here.

In this study, we implement a three-band, absorptance-only inverse Judd–Ofelt (JO) protocol and apply it to Er^{3+}, Dy^{3+}, and Sm^{3+} ions embedded in compositionally identical oxyfluoride glasses. For each ion, baseline-corrected integrated absorption band areas yield relative line strengths. These, combined with tabulated reduced matrix elements, provide (Ω_2:Ω_4:Ω_6) ratios via a linear system. A single radiative-lifetime constraint is then used to fix the absolute scale, enabling complete JO parameter sets and derived radiative descriptors to be obtained from relative spectra alone. This framework permits direct, anchor-independent comparison of JO properties across multiple RE^{3+} ions in a shared host environment. The goals are two-fold: (i) to assess the stability of the inverse JO method under fixed-lifetime scaling, and (ii) to enable consistent cross-ion spectroscopic comparisons under identical compositional and measurement conditions. In this way, the methodology supports rapid screening of new RE^{3+}-doped materials when only relative absorption data are available.

Beyond classical calibrated-absorption JO fits, calibration-light approaches include emission-based extraction (e.g., JOES) [13], self-referenced excitation normalization [14], and diffuse-reflectance/Kubelka–Munk combined with lifetimes [12,18]. Recent overviews—e.g., Hrabovský et al. [20]—also recommend using the mean emission wavelength (band barycenter) in the λ^{-3} factor and summarize practical sources of bias. Against that background, our contribution is an absorbance-only, three-band inverse protocol that: (i) determines Ω_2:Ω_4:Ω_6 from uncalibrated transmission data without d, N, or absolute intensity calibration; (ii) applies a single lifetime anchor only after inversion, making Ω-ratios and within-set fractions p_k anchor-independent; (iii) uses three well-resolved, non-overlapping bands to avoid de-overlap and arbitrary weighting inherent to multi-band fits; and (iv) reports uncertainties via resampling. This yields like-for-like cross-ion comparisons from minimal inputs in a shared host—capabilities not delivered together by existing calibration-light methods.

Regarding the scope of the inverse Judd–Ofelt framework, when absolute calibration is available (reliable d, N, n), classical JO is the preferred route; in this calibrated limit, the inverse framework recovers the same Ω-ratios and normalized descriptors. When calibration is incomplete or uncertain (archival/relative spectra, exploratory compositions, cross-lab heterogeneity), classical JO becomes under-determined or assumption-laden, whereas the inverse method provides reproducible, JO-consistent Ω-ratios and pk from relative spectra under explicit assumptions and quantified uncertainties.

2. Theory and Notation

The Judd–Ofelt (JO) theory provides a rigorous quantum mechanical description of ED transitions between 4f levels of RE^{3+} ions in glassy hosts. In practice, absorption spectra display many overlapping 4f–4f bands of varying intensity. For the inverse JO procedure adopted here, we restrict the analysis to three well-resolved ground-state absorption bands per ion, chosen for their spectral prominence, minimal overlap, and well-established assignments. To avoid ambiguity, we denote these bands by the index k and define the restricted set S = {1, 2, 3}. All sums $\sum_{k\in S}$ are confined to this subset. Within this framework, the normalized ED fractions p_k are defined only across S and must not be confused with branching ratios β, which apply when all possible radiative channels are considered.

2.1. JO Relations (ED Line Strength, Radiative Rate, Branching)

For an electric–dipole (ED) 4f–4f transition from the upper (emitting) manifold $|J_u\rangle$ to a lower manifold $|J_\ell\rangle$, the line strength is:

$$S_{\mathrm{ED}}(J_u \to \mathrm{J}_\ell) = \sum\nolimits_{t=2,4,6} \Omega_t \cdot \left|\langle J_u \| U^{(t)} \| \mathrm{J}_\ell\rangle\right|^2, \tag{1}$$

where Ω_t(t = 2,4,6) are the JO intensity parameters and $\langle J_u \| U^{(t)} \| \mathrm{J}_\ell\rangle$ are reduced matrix elements tabulated for RE^{3+} ions [10]. Equivalently, for absorption $(J_g \to \mathrm{J}_u)$, the same S_{ED} enters with $\left|J_g \middle\| U^{(t)} \middle\| \mathrm{J}_u\rangle\right|^2$; the two forms are identical in modulus-squared.

The corresponding Einstein radiative rate (spontaneous emission probability) follows as:

$$A_{\mathrm{rad}}(J_u \to J_\ell) = \frac{64e^2\pi^4}{3h(2J_u+1)} L(n)\,.\,\lambda^{-3}\,.\,S_{\mathrm{ED}}(J_u \to J_\ell),\; L(n) = \frac{n\left(n^2+2\right)^2}{9} \tag{2}$$

which links the ED line strength to the spontaneous-emission probability: given S_{ED} and λ, it returns the physical A_{rad}. Here, e is the elementary charge, h is Planck's constant, n is the host refractive index, λ is the emission wavelength of the transition (approximated here by the absorption maximum, $\lambda_{\mathrm{em}} \approx \lambda_{\mathrm{abs}}$), the factor $1/(2J_u+1)$ and the Lorentz (virtual-cavity) local-field factor $L(n) = n\left(\frac{n^2+2}{3}\right)^2$, appropriate for dipoles embedded in a homogeneous dielectric [19,21]. Magnetic–dipole contributions are neglected for the selected bands, since their estimated fraction in these oxyfluoride hosts is <10% in the relevant windows [8–10].

The total radiative lifetime τ_{rad} and branching ratio β (for a single emitting manifold J_u) are, respectively:

$$\tau_{\mathrm{rad}} = \left(\sum\nolimits_\ell A_{\mathrm{rad}}(J_u \to J_\ell)\right)^{-1} \tag{3}$$

$$\beta(J_u \to J_\ell) = \frac{A_{\mathrm{rad}}(J_u \to J_\ell)}{\sum_\ell A_{\mathrm{rad}}(J_u \to J_\ell)} \tag{4}$$

We use β (branching ratio) only for decays from a single emitting manifold. For the three ground-state channels per ion (set S), we report normalized ED shares p_k

$$p_k = A_\mathrm{rad}\left(J_{u,k} \rightarrow J_g\right) / \sum\nolimits_{m\in S} A_\mathrm{rad}\left(J_{u,m} \rightarrow J_g\right) \tag{5}$$

which are dimensionless, scale-invariant, and defined only within S (not β).

For clarity, for S = {1, 2, 3}:

$$p_1 = \frac{A_\mathrm{rad}\left(J_{u,1} \rightarrow J_g\right)}{A_\mathrm{rad}\left(J_{u,1} \rightarrow J_g\right) + A_\mathrm{rad}\left(J_{u,2} \rightarrow J_g\right) + A_\mathrm{rad}\left(J_{u,3} \rightarrow J_g\right)} \tag{5a}$$

$$p_2 = \frac{A_\mathrm{rad}\left(J_{u,2} \rightarrow J_g\right)}{A_\mathrm{rad}\left(J_{u,1} \rightarrow J_g\right) + A_\mathrm{rad}\left(J_{u,2} \rightarrow J_g\right) + A_\mathrm{rad}\left(J_{u,3} \rightarrow J_g\right)} \tag{5b}$$

$$p_3 = \frac{A_\mathrm{rad}\left(J_{u,3} \rightarrow J_g\right)}{A_\mathrm{rad}\left(J_{u,1} \rightarrow J_g\right) + A_\mathrm{rad}\left(J_{u,2} \rightarrow J_g\right) + A_\mathrm{rad}\left(J_{u,3} \rightarrow J_g\right)} \tag{5c}$$

Importantly, p_k is not the oscillator strength of atomic spectroscopy.

2.2. Inverse JO from Relative Absorption: Ratios and Absolute Scaling

Since only relative absorbance spectra are typically available (arbitrary units), the corresponding band strengths cannot yield absolute oscillator strengths directly. We therefore define $\mathrm{S}_{\mathrm{rel},k}$ (k = 1, 2, 3) as the baseline-corrected, wavenumber-integrated band area normalized within the ion (so any common Nd factor cancels). For each absorption channel $J_g \rightarrow \mathrm{J}_{u,k}$, $U_{k,t} = \left|\langle J_g \| U^{(t)} \| \mathrm{J}_{u,k}\rangle\right|^2$($t$ = 2, 4, 6) [10].

Stacking the three normalized band strengths $S_\mathrm{rel,k}$ and the three Ω_t into vectors yields the linear JO system:

$$\underbrace{\begin{bmatrix} S_\mathrm{rel,1} \\ S_\mathrm{rel,2} \\ S_\mathrm{rel,3} \end{bmatrix}}_{S_\mathrm{rel}} = \underbrace{\begin{bmatrix} |\langle J_g\|U^{(2)}\|J_{u,1}\rangle|^2 & |\langle J_g\|U^{(4)}\|J_{u,1}\rangle|^2 & |\langle J_g\|U^{(6)}\|J_{u,1}\rangle|^2 \\ |\langle J_g\|U^{(2)}\|J_{u,2}\rangle|^2 & |\langle J_g\|U^{(4)}\|J_{u,2}\rangle|^2 & |\langle J_g\|U^{(6)}\|J_{u,2}\rangle|^2 \\ |\langle J_g\|U^{(2)}\|J_{u,3}\rangle|^2 & |\langle J_g\|U^{(4)}\|J_{u,3}\rangle|^2 & |\langle J_g\|U^{(6)}\|J_{u,3}\rangle|^2 \end{bmatrix}}_{\mathrm{U}} \cdot \underbrace{\begin{bmatrix} \Omega_2 \\ \Omega_4 \\ \Omega_6 \end{bmatrix}}_{\Omega_\mathrm{rel}}, \tag{6}$$

solved by non-negative least squares (NNLS), $\widehat{\Omega} = \mathrm{argmin}_{\Omega\geq 0}\|S_\mathrm{rel} - U\Omega\|_2$, which returns scale-free JO ratios Ω_2:Ω_4:Ω_6. If a selected feature contains two partially resolved channels ($J_\mathrm{u,a}$, $J_\mathrm{u,b}$), linearity is preserved by summing areas and rows: $\mathrm{S}_\mathrm{rel,k} \leftarrow \mathrm{S}_\mathrm{rel,a} + \mathrm{S}_\mathrm{rel,b}$, and the corresponding row of U is $U_\mathrm{k,t} \leftarrow U_\mathrm{a,t} + U_\mathrm{b,t}$.

2.3. Fixing the Absolute Scale by a Lifetime Constraint

Let $\Omega_\mathrm{rel} = \left(\Omega_2^{(\mathrm{rel})}, \Omega_4^{(\mathrm{rel})}, \Omega_6^{(\mathrm{rel})}\right)$ be the (column) vector returned by Equation (6). Using Equation (2), we first form relative radiative rates.

$$A_\mathrm{rad}^{(\mathrm{rel})}\left(J_{u,k} \rightarrow J_g\right) = \kappa\left(n,\ J_{u,k}\right)\lambda_k^{-3} \cdot S_\mathrm{ED}^{(\mathrm{rel})}\left(J_{u,k} \rightarrow J_g\right), \quad S_\mathrm{ED}^{(\mathrm{rel})} = \sum\nolimits_t \Omega_t^{(rel)} U_{k,t} \tag{7}$$

i.e., the same functional form as Equation (2), but built from the relative line strengths $S_\mathrm{ED}^{(\mathrm{rel})}$ implied by Equation (6). Here, the wavelength factor in Equation (2) is evaluated, preferentially, at the band's mean emission wavelength $\langle\lambda_\mathrm{em}\rangle$ (barycenter), which is the recommended choice for the λ^{-3} dependence [11]. In our absorption-only workflow, emission barycenters are not available for all samples, so we use λ_max as a practical proxy; for intra-4f transitions in oxide/oxyfluoride glasses the Stokes shift is small, so the impact in A_rad is at the few-percent level ($\Delta A/A \approx -3\ \Delta\lambda/\lambda$), well within our reported uncertainties.

The local-field factor is included uniformly within $\kappa\left(n,\ J_{u,k}\right) = \frac{64e^2\pi^4}{3h(2J_u+1)}L(n)$. Thus, $A_{\text{rad}}^{(\text{rel})}$ has the correct ratios across the three bands, but remains in arbitrary units.

To set the absolute scale, we impose a single lifetime anchor across the triplet,

$$A_{\text{rad,tot}} = \sum_{k=1}^{3} A_{\text{rad,k}} = \frac{1}{\tau_{\text{ref}}}\ ,\ \tau_{\text{ref}} = 2\text{ ms} \tag{8}$$

which defines a global factor α, such that:

$$\alpha = \frac{\frac{1}{\tau_{\text{ref}}}}{\sum_{k\in S} A_{\text{rad,k}}^{(\text{rel})}},\quad \Omega_t = \alpha\Omega_t^{(\text{rel})},\ A_{\text{rad}}\left(J_{u,k} \to J_g\right) = \alpha A_{\text{rad}}^{(\text{rel})}\left(J_{u,k} \to J_g\right) \tag{9}$$

(note that p_k is invariant to τ_{ref}).

The chosen anchor τ_{ref} = 2 ms lies within the ms-scale lifetimes reported for $^4I_{13/2}$ (Er^{3+}), $^4F_{9/2}$ (Dy^{3+}), and $^4G_{5/2}$ (Sm^{3+}) in related glasses [22–26] and is used solely to set the absolute scale.

This constraint is purely operational: it does not represent the true τ_{rad} of a single emitting manifold but enforces a uniform absolute scale. As a direct consequence of the scaling procedure, the calculated radiative lifetime τ_{rad} from the Einstein coefficients equals the imposed anchor τ_{ref}. Thus, $A_{\text{rad,k}}^{(\text{rel})}$ denote scale-free relative coefficients, while $A_{\text{rad,k}}$ are their absolute counterparts after applying α.

Summary of Scaling Logic

Starting from relative absorption areas, Equation (6) is solved by NNLS to obtain the scale-free JO parameters Ω_{rel}. Using Equation (2) with the relative line strengths implied by Equation (6), we form the relative rates $A_{\text{rad}}^{(\text{rel})}\left(J_{u,k} \to J_g\right)$ (Equation (7)), which carry the correct inter-band ratios but remain in arbitrary units. A single lifetime anchor is then imposed across the triplet, $\sum_{k=1}^{3} A_{\text{rad,k}} = \frac{1}{\tau_{\text{ref}}}$ (Equation (8)), which defines the global scale α converting Ω_{rel} and $A_{\text{rad}}^{(\text{rel})}$ into their absolute counterparts (Equation (9)). As imposed by the method, the τ_{rad} computed from the scaled A_{rad} equals τ_{ref}. The JO ratios (Ω_2:Ω_4:Ω_6) and the normalized fractions p_k are anchor-independent; only absolute magnitudes rescale.

2.4. Assumptions and Physical Validity

- Physical grounding of the inverse JO approach: The inverse route does not modify JO physics; it only changes the data normalization. The integrated absorbance areas S_k of ground-state bands are proportional to the same electric–dipole line strengths that underlie classical JO, i.e., $S_k \propto \sum_{t\in\{2,4,6\}} \Omega_t \left\langle U^{(t)}\right\rangle_k^2$, up to a single global prefactor (thickness, dopant density, detector gain, local-field). That prefactor multiplies all bands equally and therefore sets only the absolute scale of (Ω_2, Ω_4, Ω_6). Ratios such as $h = \Omega_2/(\Omega_4 + \Omega_6)$ and $\chi = \Omega_4/\Omega_6$, and within-set normalized fractions p_k, remain invariant and retain their physical meaning (e.g., hypersensitivity, medium-range rigidity, branching trends). Selection rules, local-field modeling, and Einstein relations are exactly those of classical JO; we simply exploit the scale-independence of the ratios to work with relative spectra.
- Electric–dipole (ED) dominance: The three bands per ion are ED-allowed in these hosts; magnetic–dipole (MD) terms are neglected within the chosen windows. This is standard for the selected manifolds in oxide/oxyfluoride glasses and within our uncertainty budget [8–10,25]. For the selected bands in these oxyfluoride glasses, magnetic–dipole (MD) contributions are estimated to remain below ~10% [8–10,25]. Within this uncertainty budget they are neglected here, although the framework allows their inclusion whenever significant.

- Small Stokes shift: For intra-4f transitions we take $\lambda_{em} \approx \lambda_{abs}$ in the λ^{-3} factor of Equation (2); the resulting bias is sub-dominant relative to baseline/window choices used to form $S_{rel,k}$ (Section 3.1.1). The Einstein-rate scaling with λ^{-3} follows standard radiative-rate formulas [27].
- Local-field model: We adopt the virtual-cavity factor $L(n) = n\left(\frac{n^2+2}{3}\right)^2$, with a representative visible-wavelength refractive index n = 1.52 for these oxyfluoride glasses [28], consistent with typical values in related hosts and borosilicate-crown standards [29,30]. Varying n within 1.50–1.55 changes $L\ (n)$ by ≈ 11% (about +4% from 1.50→1.52), which only rescales absolute A_{rad}; the normalized fractions p_k and the JO ratios are unaffected.
- Minimal determinacy and stability: With three bands and three Ω_t, Equation (6) is minimally determined. Stability relies on the linear independence of the rows of U (each defined by $U_{k,t}$); conditioning is verified before scaling. Solver choices and diagnostics (non-negative least squares, residual norms, condition numbers) are detailed in Section 3.1.

The workflow, summarized in Figure 1, converts relative absorption areas into Ω-ratios via tabulated reduced matrix elements, and scales them through a single lifetime anchor. This yields physically meaningful JO parameters and radiative descriptors directly from uncalibrated spectra.

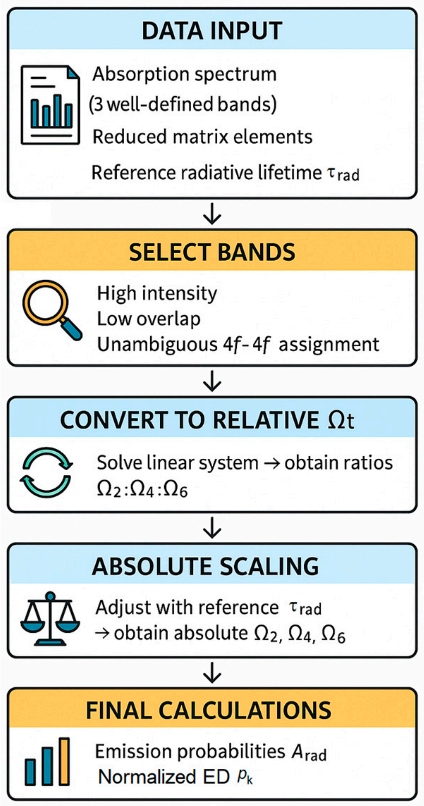

Figure 1. Workflow of the inverse Judd–Ofelt analysis.

3. Experimental

3.1. Computational Methodology

3.1.1. Spectral Preprocessing and Band Integration

The workflow in Figure 1 was applied to the Er^{3+}, Sm^{3+}, and Dy^{3+} absorption spectra acquired as (λ, Abs(λ)) in relative absorbance. Each spectrum was used on its native sampling; only when spacing irregularities compromised numerical stability did we apply a light linear interpolation to a 1–2 nm grid.

For every selected band, two short side windows bracketing the maximum defined a local linear baseline $\hat{b}(\lambda)$ (robust fit); this baseline was subtracted so that the subsequent integration reflects the physical line shape rather than slow background variations.

Because oscillator strengths are proportional to the wavenumber integral, band areas were computed in $\tilde{\nu} = 1/\lambda$ rather than in wavelength. Practically, we evaluate the wavenumber integral (implemented on the wavelength grid) using $\mathscr{A}_k = \int_{\tilde{\nu}_1}^{\tilde{\nu}_2} \left[Abs\left(\tilde{\nu}\right) - \hat{b}\left(\tilde{\nu}\right)\right] d\tilde{\nu} = \int_{\lambda_2}^{\lambda_1} \left[Abs(\lambda) - \hat{b}(\lambda)\right] \lambda^{-2} d\lambda$, where $d\tilde{\nu} = -\lambda^{-2} d\lambda$, hence the reversed wavelength limits ($\lambda_2 < \lambda_1$). The integral was evaluated over a symmetric window centered at the maximum, using the composite trapezoidal rule, yielding a baseline-corrected band area $\mathscr{A}_k$ (a.u. × nm^{-1}).

To remove the arbitrary vertical scale of each spectrum, the three areas for a given ion were normalized by the largest:

$$S_{\mathrm{rel},k} = \frac{\mathscr{A}_k}{max_m \mathscr{A}_m}, k = 1, 2, 3. \tag{10}$$

Thus, $S_{\mathrm{rel,k}}$ is normalized integrated absorption areas per ion. Although derived from relative areas, they play the role of normalized strengths in the JO inversion and preserve the Ω_2:Ω_4:Ω_6 ratios.

3.1.2. Inverse JO Analysis from Normalized Areas

The squared reduced matrix elements $\left|\left\langle J_g \middle\| U^{(t)} \middle\| J_u \right\rangle\right|^2$(t = 2, 4, 6) [10] populate the 3 × 3 design matrix U in Equation (6). The spectral weights are the three $S_{\mathrm{rel,k}}$. If a feature comprises two partially resolved channels, both the baseline-corrected sub-areas are summed, and the corresponding JO rows are added (Section 2.2).

Robustness was assessed via Monte Carlo on S_{rel} with ±7% multiplicative jitter and total-area renormalization; [2.5%, 97.5%] intervals for h and χ were computed from n = 1000 resamples.

In all cases, we verify identifiability via full rank and report the 3 × 3 condition number of U. Robustness is quantified for the anchor-independent descriptors $h = \Omega_2/(\Omega_4 + \Omega_6)$ and $\chi = \Omega_4/\Omega_6$ under light multiplicative jitter of the band areas S_{rel} (Gaussian, $\sigma \approx 7\%$) and small baseline/window perturbations. The resulting ranges [min, max] are reported in Supplementary Table S1, with graphical summaries in Supplementary Figures S1 and S2.

The 3 × 3 condition number is computed from the tabulated $\langle U^{(t)} \rangle^2$ of the selected ground-state transitions only; it does not depend on absolute scaling or on the lifetime anchor. It therefore quantifies the physics-imposed information content of the band set (selection rules and intensity pattern) rather than introducing an adjustable mathematical parameter.

The system $S_{rel} = \mathrm{U}\Omega_{rel}$ was solved by non-negative least squares (NNLS), enforcing $\Omega_t \geq 0$. Conditioning of U was monitored; if the system was ill-conditioned or the residual was dominated by a single equation, integration limits were slightly adjusted—remaining within the same physical band and without violating the selection criteria—or, where necessary, a different well-resolved band was chosen to improve linear independence. This step yields Ω_{rel}, which encodes the ratios Ω_2:Ω_4:Ω_6, but remains undetermined by a common scale. As in classical and combinatorial JO analysis, band choice influences the extracted Ω_t. To mitigate this, we restrict the inversion to three well-resolved, non-overlapping ground-state transitions, and quantify uncertainty by Monte Carlo resampling.

In terms of band selection and conditioning, we restrict the inversion to three well-resolved ground-state bands per ion to ensure a full-rank system and a numerically wellconditioned 3 × 3 inversion. In relative absorbance, adding partially overlapping bands requires explicit de-overlap and per-band weighting; in the absence of a calibrated noise model, this can bias Ω_t and degrade conditioning. Our three-band design is therefore a robustness choice for identifiability with relative spectra. Where absolutely calibrated spectra and defensible weights are available, the framework can be extended to a weighted multi-band fit.

For definiteness, the ground-state bands entering Equation (6) were: for Er^{3+} ($^4I_{15/2} \rightarrow {}^4F_{7/2}$, $^2H_{11/2}$, $^4I_{11/2}$); for Sm^{3+} ($^6H_{5/2} \rightarrow {}^6F_{7/2}$, $^6F_{5/2}$, $^6F_{3/2}$); and for Dy^{3+} ($^6H_{15/2} \rightarrow {}^6F_{5/2}$, $^6F_{7/2} + {}^6H_{5/2}$, $^6F_{11/2} + {}^6H_{9/2}$). For Dy^{3+}, two of the selected bands involve close pairs of upper levels; each feature was integrated as a single line, and the corresponding JO row in U was taken as the sum of the two-level rows ($^6F_{7/2}$ and $^6H_{5/2}$; $^6F_{11/2}$ and $^6H_{9/2}$), which preserves Equation (6) exactly.

3.1.3. Scaling and Uncertainty Analysis

Band sufficiency and identifiability: Three well-resolved ground-state bands per ion suffice because the 3 × 3 JO system is identifiable when the rows of U are linearly independent and the 3 × 3 condition number is moderate.

Zero/near-zero entries in $\langle U^{(t)} \rangle^2$: Zero or near-zero reduced-matrix elements in one or two bands do not preclude inversion. Identifiability is governed by full rank and conditioning of U; if U is full rank (e.g., a non-zero 2 × 2 minor among the U_4 and U_6 columns together with at least one non-zero U_2 entry), the solution remains well posed. This is reflected in the reported condition numbers and the jitter-based robustness ranges (Supplementary Table S1; Figures S1 and S2).

Diagnostics and robustness: Complete numerical diagnostics are provided in Supplementary Table S1 and summarized in Supplementary Figures S1 and S2: 3 × 3 condition number, h, χ and [2.5%, 97.5%] robustness intervals obtained under ±7% multiplicative jitter of S_{rel}, with renormalization of the total band area and small baseline/window perturbations modeled by the jitter. All robustness results were computed with $n = 1000$ Monte Carlo resamples. An analytical proof that the ratios and p_k are invariant to global intensity rescaling is given in Appendix A.

Interpreting the robustness intervals: The reported [2.5%, 97.5%] bounds are percentiles of the Monte Carlo distribution (central 95% interval) rather than percentages of the nominal value. Narrow intervals indicate good numerical conditioning and low sensitivity to spectral perturbations; wider intervals reflect a more sensitive yet still identified 3 × 3 system under ±7% multiplicative jitter of $S_{re}l$ with total-area renormalization.

The absolute scale follows Section 2.3, enforcing, for the three selected ground-state absorption transitions per ion (set S), the constraint $A_{rad,tot} = 500\ s^{-1}$ ($\tau_{ref} = 2$ ms), which defines the single factor α given by Equation (8). With the JO parameters Ω_t ($t = 2, 4, 6$) scaled, the absolute S_{ED}, A_{rad} and τ_{rad} follow from Equations (1)–(3). As terminology, we report f_k within S (β reserved for single-manifold decays; see Section 2.1).

Uncertainties were estimated by perturbing only the steps that affect relative areas:

(i) baseline fits were jittered within the local noise;
(ii) integration half-widths were randomly varied by ±(5–10) nm;
(iii) peak centers were dithered by ±2 nm to emulate discrete sampling.

In addition, we performed Monte Carlo resampling of S_{rel} by applying multiplicative Gaussian noise ($\sigma \approx 7\%$, capturing baseline/window/peak variability). For each ion, 1000 realizations were propagated through Equations (2) and (5)–(8), and the spreads of Ω_t and p_k were summarized as percentile-based 95% confidence intervals.

Under these controlled steps, the inverse JO workflow converts relative absorption data into scaled Ω_t, Einstein coefficients A_{rad}, and normalized ED fractions f_k suitable for cross-ion comparison in this specific oxyfluoride glass host.

All numerical processing was performed in Python 3.11 using *NumPy* (array handling and trapezoidal integration), *SciPy* (linear interpolation, NNLS solver, and condition-number analysis), and *pandas* (data organization and export). Random perturbations for uncertainty analysis were generated with *NumPy.random*, and the full pipeline (preprocessing → S_{rel} → NNLS → lifetime scaling) was executed reproducibly. Diagnostic plots and spectral checks were produced with *Matplotlib*.

3.2. Glass Preparation and Absorption Measurements

Oxyfluoride glasses (mol%: 60 SiO_2, 20 Al_2O_3, 10 Na_2O, 10 BaF_2) were prepared by melt–quenching. Three independent batches were produced, each doped with a single rare-earth oxide (Er_2O_3, Dy_2O_3, or Sm_2O_3) at a nominal number density $N \approx 5 \times 10^{20}$ cm^{-3}. Raw materials were of high purity: SiO_2 (≥99.5%, Sigma-Aldrich, St. Louis, MO, USA), Al_2O_3 (≥99.9%, Alfa Aesar, Ward Hill, MA, USA), Na_2CO_3 (≥99.5%, Merck, Darmstadt, Germany), BaF_2 (≥99.9%, Sigma-Aldrich), and rare-earth oxides (99.9%, Alfa Aesar). Batches of ~30–50 g were melted in a platinum crucible at 1450 °C for 1 h, cast onto a stainless-steel plate, and annealed at 500 °C for 2 h to relieve internal stress.

Specimens had thickness $d = 2.0 \pm 0.1$ mm. Room-temperature absorption spectra were recorded with a PerkinElmer Lambda 9 UV–Vis–NIR spectrophotometer (PerkinElmer, Waltham, MA, USA) over 390–1700 nm, with 2 nm spectral resolution. Data were acquired as relative absorbance (a.u.) vs. wavelength (no absolute calibration).

Radiative-rate calculations use the optical model described in Section 2.4. For each ion, three ground-state 4f→4f bands were selected based on prominence and minimal overlap (band-selection details and treatment of partially mixed features are in Sections 2.2 and 3.1).

4. Results and Discussion

The inverse Judd–Ofelt (JO) analysis yields a self-consistent set of JO (intensity) parameters (Ω_2, Ω_4, Ω_6) and derived radiative quantities for Er^{3+}, Sm^{3+}, and Dy^{3+} embedded in the same oxyfluoride glasses under uniform optical assumptions (see Section 2.4). Only the normalized strengths $S_{rel,k}$ enter the inversion (NNLS); the absolute scale is fixed as described in Section 2.3. Uncertainties are reported as 95% confidence intervals from resampling of S_{rel} ($\sigma \approx 7\%$, Section 3.1.3). Normalized quantities—the JO ordering (Ω_2:Ω_4:Ω_6) and p_k—are anchor-independent (see Section Summary of Scaling Logic). We also use anchor-independent JO metrics (normalized Ω vectors and the indices $\chi = \Omega_4/\Omega_6$, $h = \Omega_2/(\Omega_4 + \Omega_6)$) to aid cross-ion interpretation.

In what follows, we first comment on the absorption features (Figures 2–4, Tables 1–3), then discuss the extracted JO parameters (Table 4) and radiative outputs (Table 5), and finally assess robustness, limitations, and implications.

Table 1. Er^{3+}: integrated areas $\mathscr{A}_k$, normalized strengths $S_{rel,k}$, and squared reduced matrix elements $|\langle U^{(t)}\rangle|^2$ of the three selected peaks [10].

Peak	l (nm)	Electronic Transition	Integrated Area ($\mathscr{A}_k$) ($\times 10^{-6}$ a.u./nm)	$S_{rel,k}$	$\langle U^{(2)}\rangle^2$	$\langle U^{(4)}\rangle^2$	$\langle U^{(6)}\rangle^2$
1	487	$^4I_{15/2} \to {}^4F_{7/2}$	3.224	0.467	0.0	0.1465	0.6272
2	521	$^4I_{15/2} \to {}^2H_{11/2}$	6.908	1.00	0.7158	0.4138	0.0927
3	974	$^4I_{15/2} \to {}^4I_{11/2}$	1.169	0.169	0.0276	0.0002	0.3942

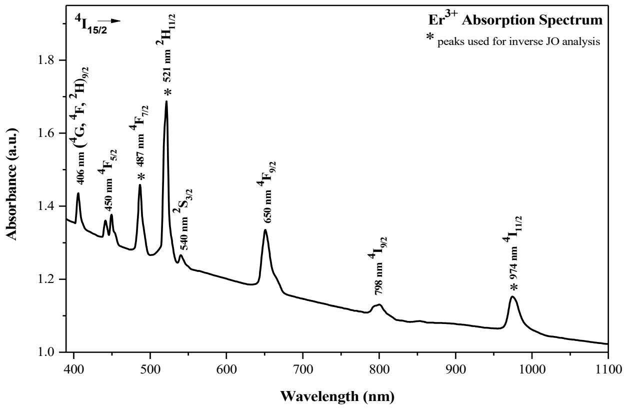

Figure 2. Er^{3+} absorption spectrum. Selected bands (set S) are marked with *.

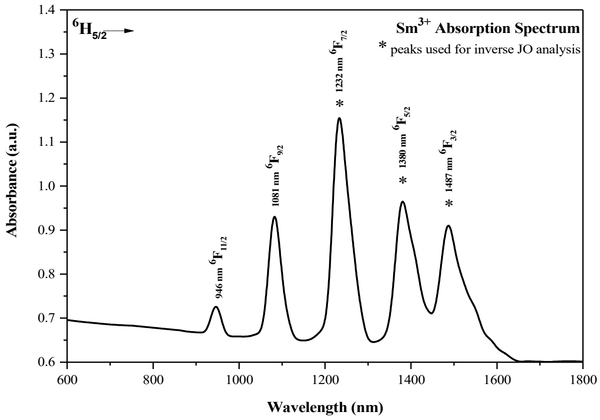

Figure 3. Sm^{3+} absorption spectrum. Selected bands (set S) are marked with *.

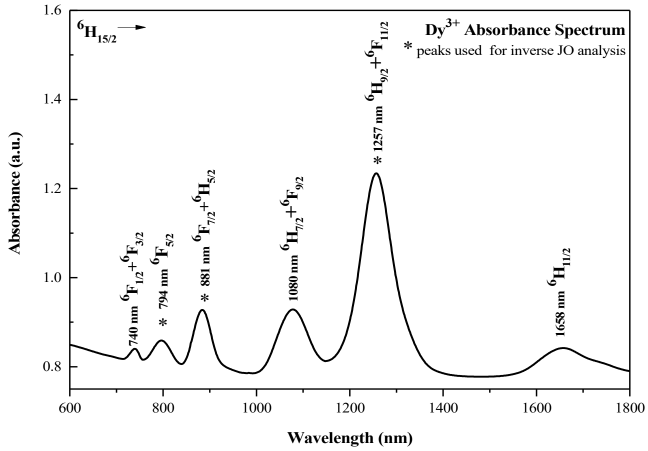

Figure 4. Dy^{3+} absorption spectrum. Selected bands (set S) are marked with *.

Table 2. Sm^{3+}: integrated areas $\mathscr{A}_k$, normalized strengths $S_{rel,k}$, and squared reduced matrix elements $|\langle U^{(t)} \rangle|^2$ of the three selected peaks [10].

Peak	l (nm)	Electronic Transition	Integrated Area ($\mathscr{A}_k$) ($\times 10^{-6}$ a.u./nm)	$S_{rel,k}$	$\langle U^{(2)} \rangle^2$	$\langle U^{(4)} \rangle^2$	$\langle U^{(6)} \rangle^2$
1	1232	$^6H_{5/2} \rightarrow ^6F_{7/2}$	1.843	1.0	0.0020	0.1429	0.4301
2	1380	$^6H_{5/2} \rightarrow ^6F_{5/2}$	0.822	0.446	0.0331	0.2844	0.0
3	1487	$^6H_{5/2} \rightarrow ^6F_{3/2}$	0.706	0.383	0.1444	0.1365	0.0

Table 3. Dy^{3+}: integrated areas $\mathscr{A}_k$, normalized strengths $S_{rel,k}$, and squared reduced matrix elements $|\langle U^{(t)}\rangle|^2$ of the three selected peaks [10].

Peak	l (nm)	Electronic Transition	Integrated Area ($\mathscr{A}_k$) ($\times 10^{-6}$ a.u./nm)	$S_{rel,k}$	$\langle U^{(2)}\rangle^2$	$\langle U^{(4)}\rangle^2$	$\langle U^{(6)}\rangle^2$
1	794	$^6H_{15/2}\rightarrow{}^6F_{5/2}$	0.154	0.092	0.0	0.0	0.3446
2	881	$^6H_{15/2}\rightarrow{}^6F_{7/2}+{}^6H_{5/2}$	0.412	0.246	0.0	0.1352	0.7164
3	1257	$^6H_{15/2}\rightarrow{}^6F_{11/2}+{}^6H_{9/2}$	1.673	1.0	0.9394	0.8465	0.4078

Table 4. Inverse JO intensity parameters (Ω_2, Ω_4, Ω_6).

Ion	Ω_2 ($\times 10^{-20}$ cm^2)	Ω_4 ($\times 10^{-20}$ cm^2)	Ω_6 ($\times 10^{-20}$ cm^2)
Dy^{3+}	4.910	3.368	2.246
Sm^{3+}	0.193	2.040	1.388
Er^{3+}	2.257	3.380	0.700

Table 5. JO-derived electric–dipole (ED) radiative rates and normalized ED fractions for the three selected ground-state transitions per ion. Calculations use optical model as in Section 2.4; absolute scaling as in Section 2.3. p_k are normalized within set S (not single-manifold branching ratios; see Section 2.1), and 95% CIs via Monte Carlo resampling of S_{rel} (see Section 3.1.3). As imposed by the method, $f_1 + f_2 + f_3 = 1.000$ (differences only from rounding).

Ion	Electronic Transition	λ (nm)	S_{ED} ($\times 10^{-20}$ cm^2)	A_{rad} (s^{-1})	95% CI on A_{rad}	p_k	95% CI on p_k	$A_{rad,tot}$ (s^{-1})
Er^{3+}	$^4I_{15/2}\rightarrow{}^4F_{7/2}$	487	0.934	133.9	116.3–153.2	0.268	0.233–0.306	500
Er^{3+}	$^4I_{15/2}\rightarrow{}^2H_{11/2}$	521	3.079	360.1	340.2–378.0	0.720	0.680–0.756	
Er^{3+}	$^4I_{15/2}\rightarrow{}^4I_{11/2}$	974	0.339	6.0	4.5–7.6	0.012	0.009–0.015	
Sm^{3+}	$^6H_{5/2}\rightarrow{}^6F_{7/2}$	1232	0.889	102.3	91.1–113.6	0.205	0.182–0.227	500
Sm^{3+}	$^6H_{5/2}\rightarrow{}^6F_{5/2}$	1380	0.587	258.7	246.0–270.9	0.517	0.492–0.542	
Sm^{3+}	$^6H_{5/2}\rightarrow{}^6F_{3/2}$	1487	0.306	139.0	124.0–154.0	0.278	0.248–0.308	
Dy^{3+}	$^6H_{15/2}\rightarrow{}^6F_{5/2}$	794	0.774	88.3	75.0–102.3	0.177	0.150–0.205	500
Dy^{3+}	$^6H_{15/2}\rightarrow{}^6F_{7/2}+{}^6H_{5/2}$	881	2.064	171.7	152.6–190.8	0.343	0.305–0.382	
Dy^{3+}	$^6H_{15/2}\rightarrow{}^6F_{11/2}+{}^6H_{9/2}$	1257	8.379	240.0	218.7–260.9	0.480	0.437–0.522	

4.1. Absorption Features

The room-temperature absorption spectra across the UV–NIR window of the three samples, each doped with 5×10^{20} cm^{-3} of the respective RE^{3+}, are shown in Figure 2 (Er^{3+}), Figure 3 (Sm^{3+}), and Figure 4 (Dy^{3+}). Spectra are presented in relative absorbance. Transition assignments follow the standard free-ion multiplet scheme (Dieke's diagram [31]) and the reduced-matrix-element compilation of Carnall et al. [10], and are consistent with prior reports for related glass hosts [32–36]. Comparing the three spectra, a clear pattern emerges: Er^{3+} concentrates oscillator strength in the UV/visible, whereas Sm^{3+} and Dy^{3+} display comparatively stronger near-IR manifolds—again in line with the literature [32–36]. Band integration followed the methodology in Section 3.1.1.

Guided by the criteria in Section 3, we retained three ground-state bands per ion (see Section 2 for the definition of S). The integrated areas $\mathscr{A}_k$, $S_{rel,k}$, and matrix elements $|\langle U^{(t)}\rangle|^2$ (t = 2, 4, 6) appear in Tables 1–3 as input to Equation (6). The selected peaks are explicitly highlighted in Figures 2–4.

For Er^{3+} (Figure 2), the visible features near ∼487, ∼521, and ∼974 nm are assigned to $^4I_{15/2}\rightarrow{}^4F_{7/2}$, $^2H_{11/2}$, and $^4I_{11/2}$, respectively, consistent with oxide/fluoride-containing glass spectra [33,37–39]. These transitions are well separated, enabling reliable baseline subtraction and integration.

Table 1 lists the integrated areas, normalized strengths, and corresponding matrix elements.

For Sm^{3+} (Figure 3), the spectrum from the $^6H_{5/2}$ ground state shows the expected ladder of near-IR ^6F_J transitions. The three retained bands, centered at ∼1232, 1380, and 1487 nm, align with previous glass studies [34,35]. Table 2 summarizes the integrated areas, normalized strengths ($\mathscr{A}_k$, $S_{rel,k}$), and $|\langle U^{(t)}\rangle|^2$.

For Dy^{3+} (Figure 4), from $^6H_{15/2}$ the three selected bands lie at ∼794 nm, 881 nm, and 1257 nm. The ∼881 nm feature is commonly assigned to a close pair $^6F_{7/2}$ + $^6H_{5/2}$, and the ∼1257 nm feature to $^6F_{11/2}$ + $^6H_{9/2}$ in glass hosts [40–43]; here, it is integrated as a single band (Section 3.2), with linearity preserved by summing sub-areas and the corresponding rows of U. The numerical inputs ($\mathscr{A}_k$, $S_{rel,k}$, and $|\langle U^{(t)}\rangle|^2$) are given in Table 3.

For each set of squared reduced matrix elements $\langle U^{(t)}\rangle^2$ used in the JO analysis, the numerical values were taken directly from Carnall's tabulations for LaF_3 [10]. These tabulated values provide the $U_{k,t}$ coefficients that populate the design matrix U in Equation (6).

Taken together, the bands highlighted in Figures 2–4 and quantified in Tables 1–3 define, for each ion, the set S used in the inversion. The qualitative contrast observed here—visible-dominated Er^{3+} versus near-IR-dominated Sm^{3+}—propagates quantitatively to the JO parameters and, ultimately, to the normalized radiative fractions p_k.

For completeness, we note that the selected sets include ΔJ = 2 channels (e.g., Dy^{3+}: $^6F_{11/2}$; Er^{3+}: $^2H_{11/2}$, $^4I_{11/2}$), which are classically regarded as hypersensitive [44,45]; their relative weights are discussed in Section 4.2.

4.2. JO Intensity Parameters: Trends and Host Interpretation

The lifetime-scaled JO parameters obtained by the inverse procedure (Table 4) lie within customary ranges for RE-doped oxide/oxyfluoride hosts and show the expected sensitivity to local structure [9,35,36,42,44]. The obtained Ω_t values fall within ranges reported for oxyfluoride hosts and reproduce the known ordering trends across ions [37–39,42,45]. While combinatorial JO analysis provides an alternative route [13,14], our protocol is complementary, tailored for cases where only relative spectra are available.

Two salient features are observed (structural trends). First, Ω_2—widely used as an indicator of site asymmetry and 4f–ligand covalency—follows $Dy^{3+} > Er^{3+} > Sm^{3+}$, with values Ω_2 = 4.910, 2.257, and 0.193 ($\times 10^{-20}$ cm^2), respectively. This ranking is consistent with stronger symmetry breaking and/or greater RE–O character around Dy^{3+}, and a comparatively more centrosymmetric, more ionic (RE–F-weighted) environment around Sm^{3+} in these glasses [9,36,42–45]. Second, the empirical rule $\Omega_4 > \Omega_6$ holds for all three ions (Er^{3+}: 3.380 > 0.700; Sm^{3+}: 2.040 > 1.388; Dy^{3+}: 3.368 > 2.246, in $\times 10^{-20}$ cm^2), in line with reports for oxide-leaning networks where the medium-range rigidity sensed by Ω_4 exceeds the longer-range polarizability captured by Ω_6 [35,36,42,44]

For anchor-independent comparison, we also consider anchor-independent metrics. With sum-normalization $(\Omega_2, \Omega_4, \Omega_6)/\sum\Omega_t$, the resulting normalized vectors are Er^{3+} (0.356, 0.533, 0.110), Sm^{3+} (0.053, 0.563, 0.383), and Dy^{3+} (0.467, 0.320, 0.213). The quality factor $\chi = \Omega_4/\Omega_6$ is 4.83 (Er^{3+}), 1.50 (Dy^{3+}), 1.47 (Sm^{3+}), while the hypersensitivity index $h = \Omega_2/(\Omega_4 + \Omega_6)$ is 0.875 (Dy^{3+}), 0.553 (Er^{3+}), 0.056 (Sm^{3+}). Together, these descriptors substantiate that Dy^{3+} exhibits the strongest site-asymmetry response (Ω_2 and h largest), Er^{3+} displays a comparatively rigid intermediate-range response (χ largest, Ω_6 smallest), and Sm^{3+} retains the most symmetric/least covalent local environment (Ω_2 smallest) in this oxyfluoride host [42].

The present composition (mol%: 60 SiO_2, 20 Al_2O_3, 10 Na_2O, 10 BaF_2) is oxide-leaning but fluorine-bearing. In such networks, (i) F^- lowers covalency and often reduces Ω_2 relative to purely oxide hosts, especially when RE–F contacts prevail [36,44,45]; (ii) Na_2O introduces non-bridging oxygens (NBOs) that can increase site asymmetry and promote

RE–O coordination when RE^{3+} resides near modifier-rich regions [4,35]; (iii) Al_2O_3 increases cross-linking/field strength and contributes to intermediate-range rigidity, which tends to elevate Ω_4 over Ω_6 [4,35]; and (iv) BaF_2 supplies F while its heavy cation enhances local field, but only modestly affects polarizability compared with high-index heavy-metal oxides. Within this framework, the very small Ω_2 of Sm^{3+} suggests that Sm^{3+} sites in this glass are on average more symmetric and more ionic, plausibly with a higher F share in the first coordination shell and/or fewer nearby NBOs. By contrast, the large Ω_2 of Dy^{3+} points to stronger symmetry breaking and greater RE–O mixing, consistent with Dy^{3+} sampling more modifier-rich, O-bearing motifs. Er^{3+} lies in between for Ω_2 but shows the largest χ, indicating that the network's intermediate-range stiffness (to which Ω_4 is sensitive) is particularly effective around Er^{3+}—a behavior often reported for aluminosilicate-rich matrices [4,35–37], where Al–O cross-linking is significant. Therefore, the pattern $\Omega_4 > \Omega_6$ across all ions is fully consistent with an oxide-dominated backbone modulated by fluorine, i.e., an oxyfluoride with lower covalency than pure oxides, yet greater rigidity than fluoride-rich glasses [35,42,44].

Three internal checks reinforce this interpretation: (i) all Ω_t are positive and fall within customary ranges for oxide/oxyfluoride glasses; (ii) the ordering Ω_2 (Dy^{3+}) > Ω_2 (Er^{3+}) > Ω_2 (Sm^{3+}) mirrors the prominence of hypersensitive (DJ = 2) channels noted in Section 4.1 [42,43]; and (iii) the normalized JO vectors and the indices $\chi = \Omega_4/\Omega_6$, $h = \Omega_2/(\Omega_4 + \Omega_6)$ are invariant to the lifetime anchor and to the local-field factor (Section 2.4), providing an anchor-independent basis for cross-ion comparison under uniform optical assumptions.

4.3. Radiative Probabilities and Normalized ED Fractions P_k

Table 5 compiles the electric–dipole (ED) radiative rates and the corresponding normalized fractions for the three ground-state absorption transitions selected per ion. The ED line strengths S_{ED} were computed from the JO parameters (Table 4) and the squared reduced matrix elements (Tables 1–3), and the Einstein coefficients A_{rad} follow from Equation (2) under the optical model of Section 2.4; the absolute scale is set as in Section 2.3. In the present oxyfluoride host, these patterns should be interpreted against an oxide-leaning backbone modulated by F^- coordination and modifier-induced non-bridging oxygens (NBOs): in aluminosilicate/oxyfluoride systems, Ω_2 generally decreases with increasing fluoride character, whereas Ω_4/Ω_6 tracks intermediate-range rigidity [45]. We reiterate that the lifetime anchor τref sets only the global scale; Ω-ratios and normalized fractions pk remain invariant. Where measured lifetimes exist, they can directly replace τref, yielding ion-specific absolute values without altering cross-ion comparisons.

For Er^{3+}, the partition is dominated by the blue–green $^4I_{15/2} \rightarrow {}^2H_{11/2}$ line at 521 nm (f ≈ 0.72), with a secondary $^4I_{15/2} \rightarrow {}^4F_{7/2}$ channel at 487 nm (f ≈ 0.27); the NIR $^4I_{11/2}$ branch at 974 nm is minor (f ≈ 0.01). This reflects both the larger S_{ED} of the 521 nm band and the λ^{-3} dependence in Equation (2) [25,45], consistent with the comparatively large Ω_4/Ω_6 ratio for Er^{3+}. For Sm^{3+}, the near-IR set favors $^6F_{5/2}$ at 1380 nm (f ≈ 0.52), followed by $^6F_{3/2}$ at 1487 nm (f ≈ 0.28) and $^6F_{7/2}$ at 1232 nm (f ≈ 0.21). For the very small Ω_2 together with moderate Ω_4, Ω_6 (Table 4) is compatible with more ionic, more symmetric local fields—plausibly a higher RE–F share and/or fewer nearby NBOs typical of oxyfluoride environments [45]. Dy^{3+} exhibits the most uneven split: the mixed ~1257 nm feature ($^6F_{11/2}$ + $^6H_{9/2}$) carries ∼48% of the ED return, the 881 nm mixed line ($^6F_{7/2}$ + $^6H_{5/2}$) contributes ∼34%, and the 794 nm $^6F_{5/2}$ line accounts for ∼18%. The coexistence/mixing of the $^6F_{11/2}$ and $^6H_{9/2}$ upper terms around 1.3 μm in glasses is well documented [38–41] (integration of mixed features follows Section 3.1.2.). The prominence of Dy^{3+} at shorter wavelengths aligns with its larger Ω_2, consistent with Dy^{3+} sampling more asymmetric, O-richer modifier environments (NBO-bearing) despite the λ^{-3} penalty at longer wavelengths [38,39,45].

Uncertainties are reported in Table 5 as 95% confidence intervals (see Section 3.1.3). Typical half-widths are ~5–12% for A_{rad} and ~0.02–0.04 for $\boldsymbol{p_k}$. Because $\boldsymbol{p_k}$ depend only on relative weights, both the $\boldsymbol{p_k}$ patterns and the JO-ratio interpretations of Section 4.2 are insensitive to the lifetime anchor and to the local-field model (Section 2.3).

4.4. Cross-Ion Comparison Under Uniform Optical Assumptions

Our extracted Ωt values and relative fractions are consistent with systematic studies across different RE^{3+} ions, including oxide and fluoride hosts [37], and more recent works on fluorotellurite glasses [46] and RE-doped ceramics [47], as well as the compositional surveys of silicate, borate, and phosphate glasses by Takebe et al. [48]. These comparisons reinforce that the observed Ω_2 suppression and Ω_4/Ω_6 trends in oxyfluoride hosts are fully aligned with the broader literature.

Because all three ions were analyzed with the same optical model (see Section 2.4), the same lifetime anchor (see Section 2.3), and the same preprocessing/inversion pipeline (Sections 3.1 and 3.2), the cross-ion trends are directly comparable and, for normalized quantities, anchor-independent [19,26,27,36,39].

(i) Site asymmetry/covalency: Ω_2 follows $Dy^{3+} > Er^{3+} > Sm^{3+}$ (see Section 4.2; Table 4);

(ii) Intermediate- vs. long-range response: The empirical rule $\Omega_4 > \Omega_6$ holds for all ions (see Section 4.2; Table 4);

(iii) Radiative partitioning within the selected triplets: The normalized ED fractions p_k (Table 5) summarize how each ion distributes ED strength under identical assumptions. In brief, Er^{3+} is dominated by the blue–green ${}^4I_{15/2} \rightarrow {}^2H_{11/2}$ branch with ${}^4I_{15/2} \rightarrow {}^4F_{7/2}$ secondary and ${}^4I_{11/2}$ minor; Sm^{3+} partitions more evenly across the near-IR set, led by ${}^6F_{5/2}$ with contributions from ${}^6F_{3/2}$ and ${}^6F_{7/2}$; Dy^{3+} is most asymmetric, with the longest-wavelength mixed (${}^6F_{11/2} + {}^6H_{9/2}$) feature leading, followed by the mixed (${}^6F_{7/2} + {}^6H_{5/2}$) line and ${}^6F_{5/2}$. For numerical values and uncertainties, see Section 4.3 and Table 5.

(iv) Link to glass composition: In the $60SiO_2$–$20Al_2O_3$–$10Na_2O$–$10BaF_2$ matrix, an oxide-leaning backbone (Si–O–Al cross-linking) promotes $\Omega_4 > \Omega_6$, while F^- coordination tends to lower covalency and suppress Ω_2. The very small Ω_2 of Sm^{3+} is therefore consistent with more ionic, more symmetric local fields (greater RE–F share/fewer nearby NBOs), whereas the large Ω_2 of Dy^{3+} suggests O-richer, asymmetry-enhancing neighborhoods (modifier/NBO influence). Er^{3+} combines moderate Ω_2 with the largest χ, consistent with stiffer intermediate-range environments in this aluminosilicate-rich glass [30,35,36,44,45].

(v) Robustness: These qualitative rankings persist within the 95% confidence intervals reported in Table 5. Treating Dy^{3+} mixed features as single bands (with summed $\langle U^{(t)} \rangle^2$) preserves the linear model and does not change the ordering of Ω_t or the p_k patterns; changes to n or τ_{ref} rescale A_{rad}, but leave Ω-ratios and p_k unchanged [19,38–42].

4.5. Practical Implications

The inverse JO route gives two things straight from uncalibrated absorbance, the intensity set Ω_t and the within-set ED fractions p_k—precisely the quantities that are often available in early glass screening or when mining legacy data [12,13,17,36,42]. Because all ions were treated using the same optical model (local-field model and lifetime anchor), the JO ordering (Ω_2:Ω_4:Ω_6) and p_k support like-for-like comparisons before absolute calibration. In practice, p_k provides a compact preview of the emission partition within the chosen triplets—blue/green share for Er^{3+}, orange–red for Sm^{3+}, and blue–yellow balance for Dy^{3+}—without requiring absolute emission measurements [3,18,30,40,49].

From a host-tuning perspective, the present oxyfluoride composition ($60SiO_2$–$20Al_2O_3$–$10Na_2O$–$10BaF_2$) offers clear levers that map onto Ω_t and hence onto p_k. In oxide-leaning networks, $\Omega_4 > \Omega_6$ is expected and reflects intermediate-range rigidity [35,42,44]; increasing Al_2O_3 (cross-linking) typically raises Ω_4 relative to Ω_6 [35,36]. Adding F^- (via BaF_2 or other fluorides) tends to lower Ω_2 by reducing 4f–ligand covalency and site asymmetry [36,37,44,45,50], whereas Na_2O creates non-bridging oxygens (NBOs) that can increase Ω_2 by enhancing asymmetry and RE–O mixing [4]. Within this composition domain, our results suggest that Dy^{3+}, with the largest Ω_2, benefits from O-richer, more asymmetric neighborhoods—useful for pronounced blue/yellow pairs or high-contrast sensing [30,40,43]; Sm^{3+}, with very small Ω_2 and moderate Ω_4 and Ω6, suits smoother, more evenly shared orange–NIR partitions for broadband or multi-line emission [24,46,51]; Er^{3+} combines moderate Ω_2 with the largest $\chi = \Omega_4/\Omega_6$, indicating stiffer intermediate-range environments and stable blue/green partitions—attributes aligned with narrowband applications and, from other manifolds, communications-band applications [18,35,36,52].

At the device level, Equation (2) gives $A_{rad} \propto \lambda^{-3}\, S_{ED}$, with $S_{ED} = \sum \Omega_t \langle U^{(t)} \rangle^2$ [5,6,25,42]. For fixed matrix elements, the combination "*larger* Ω_2" + "*shorter* λ" tends to yield larger A_{rad}, providing a simple screening rule for faster radiative channels; conversely, smaller Ω_2 (as for Sm^{3+}) typically flattens the ED partition within the set when a smoother spectrum is desired. Two practical considerations are worth noting: (i) the lifetime anchor rescales all A_{rad} (but not p_k or Ω-ratios), so absolute brightness still depends on the true (radiative + non-radiative) lifetime and pump overlap [42]; (ii) host phonon energy and concentration effects (multiphonon relaxation, cross-relaxation) ultimately limit usable quantum efficiency—especially in oxide-leaning glasses and partially mitigated in oxyfluorides [4,22,37,50].

In practice, this method supports rapid screening: three well-chosen ground-state bands per ion suffice to recover Ω-ratios, S_{ED}, and p_k under a common optical model [12,13,36]. If the goal is to boost Ω_2 (e.g., stronger hypersensitive response for Dy^{3+}), compositions with more NBOs (higher Na_2O) and less F^- are indicated; if a rigid network is desired (enhanced Ω_4, suppressed Ω_6) for stable partitions as in Er^{3+}, raising Al_2O_3 at fixed SiO_2 and moderating the fluoride content is a rational path [35–37,50]. These composition$\rightarrow \Omega_t \rightarrow p_k$ links support decision-making for composition selection while keeping measurements minimal and comparable across iterations.

4.6. Limitations and Sensitivity

The absolute Einstein coefficients scale linearly with the imposed lifetime anchor ($A_{rad} \propto \tau_{ref}{}^{-1}$); as noted in Section 2.3, JO ratios and p_k are anchor-independent. Accordingly, our discussion emphasizes ratio-based quantities and cross-ion comparisons under uniform optical assumptions rather than absolute A_{rad} values [42].

Replacing λ_{max} by a barycentric wavelength in the λ^{-3} factor changes individual A_{rad} by at most a few percent ($\Delta A/A \approx -3\, \Delta\lambda/\lambda$) and leaves the JO ratios and the within-set fractions p_k within the reported 95% confidence intervals (Section 3.1.3).

Potential biases can arise from several sources. (i) Band windowing and baseline: finite windows and local backgrounds control integrated areas; we used robust baselines and Monte Carlo resampling (see Section 3.1.3) in line with best practice for JO data treatment [17,42]. (ii) Magnetic–dipole admixtures: MD terms were neglected within the selected windows; small leakage would mainly perturb A_{rad}, but has limited impact on p_k because the latter renormalize within the triplet [9,42]. (iii) Stokes shift: using $\lambda_{em} \approx \lambda_{abs}$ in the λ^{-3} factor introduces a small systematic; for intra-4f transitions in glasses this is typically subdominant to baseline/window uncertainty and is encompassed by our resampling intervals (Section 3.1.3) [36]. (iv) Local-field model and refractive index: adopting the virtual-cavity factor at a representative n rescales A_{rad} and Ω_t together but leaves Ω-ratios and p_k unchanged; moderate dispersion or n-uncertainty therefore does not alter qualitative trends [19,26,27,36]. (v) Matrix-element provenance: the squared reduced elements $\langle U^{(t)} \rangle^2$ come from standard tabulations [10]; modest host-dependent J-mixing cannot be excluded [10,28,36]. (vi) Linear determinacy and conditioning: with three bands and three Ω_t, Equation (6) is minimally determined; accuracy relies on the linear independence of the three U-rows, motivating our choice of well-separated bands [42].

Our Section 3.1.3 resampling analysis indicates that these effects are captured by the 95% confidence intervals in Tables 4 and 5 and do not overturn the qualitative trends (ordering of Ω_t; p_k patterns) [17,42].

4.7. Where This Approach Helps—And Where It Does Not

The inverse JO route is most useful when (a) spectra are available only in relative units, (b) three ground-state bands per ion are well resolved with stable baselines, and (c) a reasonable lifetime anchor can be adopted for scaling. It is not a replacement for a full absolute JO analysis when calibrated absorbance, thickness, number density, and n (λ) are known; in that regime, the classical fit remains the reference method [5,6,36]. In practice, the present workflow complements modified-JO toolkits by providing a minimal-input, physically anchored way to compare ions in a common host and to triage compositions efficiently, with the understanding that absolute brightness still depends on the true (radiative + non-radiative) lifetime, pump overlap, and concentration-dependent quenching [14,15,17,22,42].

Equivalence in the calibrated limit and complementarity: When absolute calibration is available, both classical and inverse JO solve the same linear system $A\Omega = S$; any absolute rescaling multiplies S by a global factor and leaves Ω-ratios and p_k unchanged. Thus, the inverse framework coincides with classical JO for ratios in the calibrated limit, while extending JO to the widely encountered case of relative, uncalibrated spectra. All cross-ion conclusions emphasized here are based on these anchor-independent descriptors, with conditioning and robustness explicitly reported (Supplementary Table S1; Figures S1 and S2). The formal ratio equivalence in the calibrated limit is given in Appendix A.

In our data, Sm^{3+} exhibits a low 3 × 3 condition number (cond ≈ 4), and correspondingly tight robustness intervals for h and χ (Supplementary Table S1; Figures S1 and S2). In contrast, Dy^{3+} shows a higher 3 × 3 conditioning of U (cond ≈ 31), and the resulting intervals are wider—as expected from the lower independent information across the selected transitions (set by the $\langle U^{(t)} \rangle^2$ pattern in this host, not by the inversion scheme). Interval width therefore tracks the information content of the JO matrix rather than any heuristic band-counting rule.

5. Conclusions

We present an inverse application of the Judd–Ofelt (JO) formalism that operates on relative absorption spectra and uses a single lifetime anchor to set the absolute scale. Applied to Er^{3+}, Dy^{3+}, and Sm^{3+} embedded in the same oxyfluoride glass, the workflow returns the JO parameters; the anchor-independent ordering (Ω_2:Ω_4:Ω_6) and—after scaling—absolute Ω_t magnitudes and Einstein coefficients A_{rad}. For radiative partitioning within the three selected ground-state lines per ion, we report normalized electric–dipole fractions p_k (not single-manifold branching ratios). As imposed by the method, p_k and the relative ordering of Ω_2, Ω_4, Ω_6 are anchor-independent, whereas absolute A_{rad} and Ω_t scale linearly with the chosen τ_{ref}.

Despite using uncalibrated spectra, the extracted parameters fall within established ranges for oxide-leaning/oxyfluoride hosts and reproduce ion-specific trends: Ω_2 follows $Dy^{3+} > Er^{3+} > Sm^{3+}$, and $\Omega_4 > \Omega_6$ holds for all three ions. The within-triplet p_k patterns (Er^{3+} dominated by 521 nm; Sm^{3+} more evenly split across 1232/1380/1487 nm; Dy^{3+} most asymmetric with 1257 nm > 881 nm > 794 nm) are consistent with the measured absorption and with literature expectations under similar hosts. Interpreted against the glass composition (SiO_2–Al_2O_3–Na_2O–BaF_2), these trends align with an oxide-leaning backbone (favoring $\Omega_4 > \Omega_6$), F^- coordination that suppresses Ω_2, and modifier-induced NBOs that enhance site asymmetry—yielding very small Ω_2 for Sm^{3+}, large Ω_2 for Dy^{3+}, and an intermediate, rigidity-biased response for Er^{3+}.

Uncertainty was quantified by Monte Carlo resampling on the relative band strengths (baseline, window, and peak perturbations). The resulting 95% confidence intervals for A_{rad} (typically ~5–12%) and for p_k (~0.02–0.04) indicate that our qualitative conclusions are robust to the dominant processing choices. Two caveats apply: (i) absolute metrics inherit the external lifetime and local-field model; (ii) the λ^{-3} factor uses $\lambda_{em} \approx \lambda_{abs}$, appropriate for intra-4f bands in glasses and sub-dominant to baseline/window uncertainties.

Practically, the method offers a minimal-input, uniform route to obtain JO descriptors and p_k maps from uncalibrated data, enabling like-for-like materials screening across ions and compositions before full calibration is available. Future work will extend the approach to additional ions and hosts, incorporate independent emission lifetimes and absolute absorbance to tighten the scale, and combine with structural/vibrational probes to deepen the link between local environment and optical response—thereby supporting rational host design for targeted photonic functions.

Supplementary Materials: The following supporting information can be downloaded at: https://www.mdpi.com/article/10.3390/photonics12101011/s1, Supplementary Table S1: 3 × 3 condition number; h and χ nominal values; [2.5%, 97.5%] robustness intervals; n = 1000; ±7% jitter; Supplementary Figure S1: Robustness of h; intervals shown are the [2.5%, 97.5%] percentiles; n = 1000; ±7%; Supplementary Figure S2: Robustness of χ; intervals shown are the [2.5%, 97.5%] percentiles; n = 1000; ±7%.

Author Contributions: Conceptualization, H.C.V.; methodology, H.C.V. and M.G.M.; software, R.Ö.; validation, H.C.V., M.G.M. and R.Ö.; formal analysis, H.C.V.; investigation, H.C.V.; resources, H.C.V.; data curation, M.G.M.; writing—original draft preparation, H.C.V.; writing—review and editing, H.C.V., M.G.M. and R.Ö.; visualization, H.C.V.; supervision, H.C.V. All authors have read and agreed to the published version of the manuscript.

Funding: This research received no external funding.

Institutional Review Board Statement: Not applicable.

Informed Consent Statement: Not applicable.

Data Availability Statement: No new data were created or analyzed in this study. Data sharing is not applicable to this article.

Acknowledgments: During the preparation of this manuscript, the authors used ChatGPT (OpenAI 5; version accessed August 2025) for language polishing and drafting text for a methodological flowchart (Figure 1) later redrawn by the authors. The authors have reviewed and edited all outputs and take full responsibility for the content of this publication.

Conflicts of Interest: The authors declare no conflicts of interest.

Abbreviations and Symbols (by Workflow)

Symbol/Term	Meaning (Concise)	Where Defined
$S = \{1, 2, 3\}$	Set of the three selected ground-state transitions per ion	Section 2
$S_{rel,k}$	Normalized band strength from absorption (unitless)	Section 3.1.1
$U_{k,t}$	Squared reduced matrix element for band k and rank $t \in \{2,4,6\}$	Section 2
JO	Judd–Ofelt theory/parameters	Section 2
$\Omega_t^{(rel)}$	Scale-free JO parameters from inverse NNLS	Section 2.3
NNLS	Non-negative least squares (solver for Equation (6))	Section 3.1.2
S_{ED}	Electric–dipole (ED) line strength	Section 2
$\kappa(n, J_u)$	Prefactor in Equation (2) (includes local-field and degeneracy terms)	Section 2.4
$L(n) = n\left(\frac{n^2+2}{3}\right)^2$	Virtual-cavity local-field factor	Section 2.4
$A_{rad}^{(rel)}$	Relative Einstein coefficient from Equation (2) with $\Omega^{(rel)}$	Section 2.3
τ_{ref}	Lifetime anchor used to set the absolute scale	Section 2.3
α	Global scaling factor converting relative → absolute (Ω_t,A_{rad})	Section 2.3
A_{rad}, $A_{rad,tot}$	Absolute Einstein rate; sum over S equals $1/\tau_{ref}$	Section 2.3
τ_{rad}	Radiative lifetime computed from A_{rad}	Section 2.3
ED/MD	Electric–dipole/magnetic–dipole	Section 2
β	Branching ratio (single emitting manifold only)	Section 2.1
p_k	Normalized fraction within S (not an oscillator strength)	Section 2.1
MC	Monte Carlo resampling for uncertainties	Section 3.1.3
CI 95%	Percentile-based 95% confidence interval	Section 3.1.3

Appendix A. Invariance of Omega-Ratios and Normalized Fractions

Statement and Proof

Let the integrated area of band κ be S_k. In the inverse Judd–Ofelt framework the three ground-state bands form the linear system $S = U\Omega$, i.e., $S_k = \sum_{t\in\{2,4,6\}} \Omega_t \left\langle U^{(t)} \right\rangle_k^2$, where U collects the reduced matrix-elements and Ω is the column vector $(\Omega_2, \Omega_4, \Omega_6)$.

Global intensity rescaling: If all spectra are multiplied by a common factor $\alpha > 0$ (e.g., thickness, dopant density, detector gain), then $S' = \alpha S$ while U is unchanged, so $\Omega' = \alpha\Omega$. Consequently, ratios are invariant: $\Omega_i'/\Omega_j' = \alpha\Omega_i/\alpha\Omega_j = \Omega_i/\Omega_j$. The descriptors used here—$h = \Omega_2/(\Omega_4 + \Omega_6)$ and $\chi = \Omega_4/\Omega_6$—are therefore unchanged.

Normalized fractions: Quantities normalized within a set (e.g., $p_k = S_k/\sum_m S_m$, or fractions proportional to Ω_t normalized by $\sum_t \Omega_t$) are also invariant, because the common factor cancels.

Lifetime anchor: Changing the lifetime anchor (t_{ref}) multiplies all absolute radiative rates by a common factor; Ω-ratios, h, χ, and p_k remain anchor-independent.

Scope: The argument assumes the same three bands and a full-rank 3 × 3 system. If magnetic–dipole terms are included, they augment U and Ω but do not alter the global-scaling invariance.

References

1. Auzel, F. Upconversion and anti-Stokes processes with f and d ions in solids. *Chem. Rev.* **2004**, *104*, 139–173. [CrossRef] [PubMed]
2. Binnemans, K. Interpretation of europium(III) spectra. *Coord. Chem. Rev.* **2015**, *295*, 1–45. [CrossRef]
3. Hong, Z.; Yue, H.; Lin, Z.; Luo, X.; Hou, H.; Wu, S.; Lai, F.; Wang, W.; You, W.; Huang, J. Photoluminescence properties of Dy^{3+}/Sm^{3+} co-doped gallium silicate glass–ceramics for solid-state warm white lighting. *J. Non-Cryst. Solids* **2024**, *628*, 122837. [CrossRef]

4. Blanc, W.; Choi, Y.G.; Zhang, X.; Nalin, M.; Richardson, K.A.; Righini, G.C.; Ferrari, M.; Jha, A.; Massera, J.; Jiang, S.; et al. The past, present and future of photonic glasses: A review in homage to the United Nations International Year of glass 2022. *Prog. Mater. Sci.* **2023**, *134*, 101084. [CrossRef]
5. Judd, B.R. Optical absorption intensities of rare-earth ions. *Phys. Rev.* **1962**, *127*, 750–761. [CrossRef]
6. Ofelt, G.S. Intensities of crystal spectra of rare earth ions. *J. Chem. Phys.* **1962**, *37*, 511–520. [CrossRef]
7. Reisfeld, R.; Jørgensen, C.K. *Lasers and Excited States of Rare Earths*; Springer: Berlin/Heidelberg, Germany, 1977.
8. Weber, M.J. Spontaneous emission probabilities for Sm^{3+}, Eu^{3+}, and Gd^{3+} in LaF_3. *Phys. Rev.* **1967**, *157*, 262–272. [CrossRef]
9. Jorgensen, C.K.; Reisfeld, R. Judd–Ofelt parameters and chemical bonding in lanthanide complexes and glasses. *J. Less Common Met.* **1983**, *93*, 107–112. [CrossRef]
10. Carnall, W.T.; Goodman, G.L.; Rajnak, K.; Rana, R.S. A systematic analysis of the spectra of the lanthanides doped into single crystal LaF_3. *J. Chem. Phys.* **1989**, *90*, 3443–3457. [CrossRef]
11. Hehlen, M.P.; Brik, M.G.; Krämer, K.W. 50th anniversary of the Judd–Ofelt theory: An experimentalist's view of the formalism and its application. *J. Lumin.* **2013**, *136*, 221–239. [CrossRef]
12. Xu, Q.; Zhang, Y.; Zhang, D.-L. Comment on "A universal approach for calculating the Judd–Ofelt parameters of RE^{3+} in powdered phosphors and its application for the β-$NaYF4{:}Er^{3+}/Yb^{3+}$ phosphor derived from auto-combustion-assisted fluoridation". *Phys. Chem. Chem. Phys.* **2019**, *21*, 10834–10839. [CrossRef]
13. Ćirić, A.; Stojadinović, S.; Sekulić, M.; Dramićanin, M.D. JOES: An application software for Judd–Ofelt analysis from Eu^{3+} emission spectra. *J. Lumin.* **2019**, *205*, 351–356. [CrossRef]
14. Ćirić, A.; Marciniak, Ł.; Dramićanin, M.D. Self-referenced method for the Judd–Ofelt parametrisation of the Eu^{3+} excitation spectrum. *Sci. Rep.* **2022**, *12*, 563. [CrossRef] [PubMed]
15. Neto, J.A.M.; Hewak, D.W. Application of a modified Judd–Ofelt theory to Pr^{3+} doped fluoride glasses. *J. Non-Cryst. Solids* **1995**, *183*, 201–207. [CrossRef]
16. Goldner, P.; Auzel, F. Application of standard and modified Judd–Ofelt theories to a praseodymium-doped fluorozirconate glass. *J. Appl. Phys.* **1996**, *79*, 7972–7977. [CrossRef]
17. Hien, N.T.; Kien, N.T.; Yen, V.H.; Ngoc, T.; Do, P.V.; Phuc, V.X.; Ca, N.X. Optical properties and Judd–Ofelt analysis of Dy^{3+} doped $CoAl_2O_4$ nanocrystals. *J. Lumin.* **2023**, *249*, 117245. [CrossRef]
18. Xue, S.-D.; Liu, M.-H.; Zhang, P.; Wong, W.-H.; Zhang, D.-L. Validity of Judd-Ofelt spectroscopy based on diffuse reflectance spectrum and fluorescence lifetime of phosphor. *J. Lumin.* **2020**, *224*, 117304. [CrossRef]
19. Vega, M.; Alemany, P.; Martín, I.R.; Llanos, J. Structural properties, Judd–Ofelt calculations, and near infrared to visible photon up-conversion in Er^{3+}/Yb^{3+} doped $BaTiO_3$ phosphors under excitation at 1500 nm. *RSC Adv.* **2017**, *7*, 10529–10536. [CrossRef]
20. Hrabovsky, J.; Varak, P.; Krystufek, R. LOMS.cz computational platform for high-throughput classical and combinatorial Judd-Ofelt analysis and rare-earth spectroscopy. *Sci. Rep.* **2025**, *15*, 28945. [CrossRef] [PubMed]
21. Kumar, G.M.; Rao, D.N.; Agarwal, G.S. Measurement of Local Field Effects of the Host on the Lifetimes of Embedded Emitters. *Phys. Rev. Lett.* **2003**, *91*, 203903. [CrossRef]
22. Babu, S.; Balakrishna, A.; Rajesh, D.; Ratnakaram, Y.C. Dy^{3+} doped oxy-fluoride phosphate glasses for laser materials: A photoluminescence study. *Int. J. ChemTech Res.* **2014**, *6*, 3276–3279.
23. Pradeesh, K.; Oton, C.J.; Agotiya, V.K.; Raghavendra, M.; Vijaya Prakash, G. Optical properties of Er^{3+} doped alkali chlorophosphate glasses for optical amplifiers. *Opt. Mater.* **2008**, *31*, 155–160. [CrossRef]
24. Pugliese, D.; Boetti, N.G.; Lousteau, J.; Ceci-Ginistrelli, E.; Bertone, E.; Geobaldo, F.; Milanese, D. Concentration quenching in an Er-doped phosphate glass for compact optical lasers and amplifiers. *J. Alloys Compd.* **2016**, *657*, 678–683. [CrossRef]
25. Pisarski, W.A. Judd–Ofelt Analysis and Emission Properties of Dy^{3+} Ions in Borogermanate Glasses. *Materials* **2022**, *15*, 9042. [CrossRef] [PubMed]
26. Praveena, R.; Venkatramu, V.; Babu, P.; Jayasankar, C.K. Fluorescence spectroscopy of Sm^{3+} ions in P_2O_5–PbO–Nb_2O_5 glasses. *Phys. B Condens. Matter* **2008**, *403*, 3527–3534. [CrossRef]
27. Hilborn, R.C. Einstein coefficients, cross sections, f values, dipole moments, and all that. *Am. J. Phys.* **1982**, *50*, 982–986. [CrossRef]
28. Wang, Y.; Shen, Y.; Zheng, R.-L.; Shen, J.-P.; Guo, H.-T.; Liu, C.-X. Optical characteristics of an oxyfluoride glass waveguide formed by a proton implantation. *Results Phys.* **2018**, *10*, 200–204. [CrossRef]
29. SCHOTTAG. *N-BK7® Optical Glass Data Sheet (nd = 1.51680 at 587.6 nm)*; SCHOTTAG: Mainz, Germany, 2023.
30. RP Photonics Encyclopedia. (s.d.). *Crown Glasses* (BK7 nd = 1.5168, nd = 1.5168, nd = 1.5168). Available online: https://www.rp-photonics.com/crown_glasses.html (accessed on 13 August 2025).
31. Dieke, G.H. *Spectra and Energy Levels of Rare Earth Ions in Crystals*; Interscience Publishers: New York, NY, USA, 1968.
32. Poonam Shivani Anu Kumar, A.; Sahu, M.K.; Rani, P.R.; Deopa, N.; Punia, R.; Rao, A.S. Judd–Ofelt parameterization and luminescence characterization of Dy^{3+} doped oxyfluoride lithium zinc borosilicate glasses for lasers and w-LEDs. *J. Non-Cryst. Solids* **2020**, *544*, 120187. [CrossRef]

33. Naresh, V.; Buddhudu, S. Analysis of visible–NIR emission and photoluminescence quenching in Er^{3+}:Bi_2O_3–AlF_3–TeO_2–B_2O_3 glasses. *Phys. Chem. Glas. Eur. J. Glass Sci. Technol. B* **2015**, *56*, 255–262. [CrossRef]
34. Kirdsiri, K.; Raja Ramakrishna, R.; Damdee, B.; Kim, H.J.; Kaewjaeng, S.; Kothan, S.; Kaewkhao, J. Optical and luminescence features of Sm^{3+}-doped Li_2O–MO–B_2O_3 (M = Mg/Ca/Sr/Ba) glasses for orange emission in WLEDs. *J. Alloys Compd.* **2018**, *749*, 197–204. [CrossRef]
35. Naresh, V.; Buddhudu, S. Energy-transfer-based emission spectra of (Sm^{3+}, Dy^{3+}):Li_2O–LiF–B_2O_3–CdO glasses. *J. Lumin.* **2014**, *147*, 63–71. [CrossRef]
36. Boudchicha, N.; Iezid, M.; Goumeidane, F.; Legouera, M.; Prasad, P.S.; Rao, P.V. Judd–Ofelt Analysis and Spectroscopy Study of Tellurite Glasses Doped with Rare-Earth (Nd^{3+}, Sm^{3+}, Dy^{3+}, and Er^{3+}). *Materials* **2023**, *16*, 6832. [CrossRef]
37. Tanabe, S.; Ohyagi, T.; Soga, N.; Hanada, T. Compositional dependence of Judd–Ofelt parameters of Er^{3+} ions in alkali-metal borate glasses. *Phys. Rev. B* **1992**, *46*, 3305–3310. [CrossRef]
38. Ebendorff-Heidepriem, H.; Ehrt, D.; Bettinelli, M.; Speghini, A. Effect of glass composition on Judd–Ofelt parameters and radiative decay rates of Er^{3+} in fluoride phosphate and phosphate glasses. *J. Non-Cryst. Solids* **1998**, *240*, 66–78. [CrossRef]
39. Duan, Z.; Zhang, J.; Hu, L. Spectroscopic properties Judd-Ofelt theory analysis of doped oxyfluoride silicate glass. *J. Appl. Phys.* **2007**, *101*, 043110. [CrossRef]
40. Mukamil, S.; Shahid, N.; Sarumaha, C.; Khattak, S.A.; Wabaidur, S.M.; Islam, M.A.; Kothan, S.; Shoaib, M.; Khan, I.; Ullah, I.; et al. Spectroscopic investigation of dysprosium doped bismuth-borate glasses for white light application. *Opt. Mater.* **2022**, *127*, 112291. [CrossRef]
41. Heo, J. 1.3-µm-emission properties and local structure of Dy^{3+} in chalcohalide glasses. *Comptes Rendus. Chimie* **2002**, *5*, 739–749. [CrossRef]
42. Joseph, P.A.J.; Maheshvaran, K.; Rayappan, I.A. Structural and optical studies on Dy^{3+} ions doped alkali lead borophosphate glasses for white light applications. *J. Non-Cryst. Solids* **2021**, *557*, 120652. [CrossRef]
43. Szymański, D.; Sobczyk, M. Optical and structural investigation of dysprosium doped-$Y_2Te_4O_{11}$. *J. Lumin.* **2016**, *173*, 11–18. [CrossRef]
44. Jørgensen Chr, K.; Judd, B.R. Hypersensitive pseudoquadrupole transitions in lanthanides. *Mol. Phys.* **1964**, *8*, 281–290. [CrossRef]
45. Van Deun, R.; Binnemans, K.; Görller-Walrand, C.; Adam, J.L. Judd–Ofelt intensity parameters of trivalent lanthanide ions in a $NaPO_3$–BaF_2-based fluorophosphate glass. *J. Alloys Compd.* **1999**, *283*, 59–65. [CrossRef]
46. Lalla, E.A.; Konstantinidis, M.; De Souza, I.; Daly, M.G.; Martín, I.R.; Lavín, V.; Rodríguez-Mendoza, U.R. Judd–Ofelt parameters of RE^{3+}-doped fluorotellurite glass (RE^{3+} = Pr^{3+}, Nd^{3+}, Sm^{3+}, Tb^{3+}, Dy^{3+}, Ho^{3+}, Er^{3+}, and Tm^{3+}). *J. Alloys Compd.* **2020**, *845*, 156028. [CrossRef]
47. Lu, K.; Liu, Z.; Wang, Y.; Yang, W.; Peng, H.; Ye, Y.; Shi, Y.; Qi, J.; Lu, T. Optical transmission and transition properties of lanthanide doped highly transparent $Y_2Zr_2O_7$ ceramics. *J. Alloys Compd.* **2022**, *905*, 164133. [CrossRef]
48. Takebe, H.; Nageno, Y.; Morinaga, K. Compositional Dependence of Judd-Ofelt Parameters in Silicate, Borate, and Phosphate Glasses. *J. Am. Ceram. Soc.* **1995**, *78*, 1161–1168. [CrossRef]
49. Kesavulu, C.R.; Yoo, M.Y.; Lee, J.H.; Lim, K.-S.; Dharmaiah, P.; Jayasankar, C.K.; Babu, P. Optical and upconversion properties of Er^{3+}-doped oxyfluoride transparent glass-ceramics containing SrF_2 nanocrystals. *J. Mater. Res.* **2013**, *28*, 1481–1489. [CrossRef]
50. Bansal, K.; Mishra, N.K.; Abdullahi, I.; Singh, P.J.; Tyagi, M.; Singh, S. Studies of luminescence traits and Judd–Ofelt analysis of Sm^{3+}-activated oxyfluoride glasses. *Opt. Mater.* **2024**, *147*, 114579. [CrossRef]
51. Chen, F.; Wei, T.; Jing, X.; Tian, Y.; Zhang, J.; Xu, S. Investigation of mid-infrared emission characteristics and energy transfer dynamics in Er^{3+} doped oxyfluoride tellurite glass. *Sci. Rep.* **2015**, *5*, 10676. [CrossRef] [PubMed]
52. Yamsuk, Y.; Yasaka, P.; Kaewkhao, J.; Sangwaranatee, N. Sm^{3+} ions doped zinc barium tellurite oxyfluoride glasses for laser materials. *J. Met. Mater. Miner.* **2020**, *30*, 10. [CrossRef]